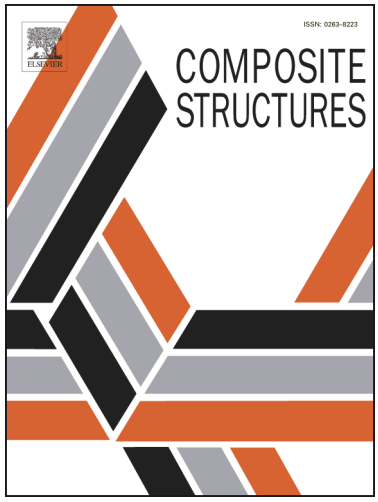

Off-axis bending behaviors and failure characterization of 3D woven composites

Diantang Zhang, Mengyao Sun, Xiaodong Liu, Xueliang Xiao, Kun Qian

PII: S0263-8223(18)30953-X
DOI: https://doi.org/10.1016/j.compstruct.2018.10.009
Reference: COST 10259

To appear in: *Composite Structures*

Received Date: 10 March 2018
Revised Date: 18 September 2018
Accepted Date: 4 October 2018

Please cite this article as: Zhang, D., Sun, M., Liu, X., Xiao, X., Qian, K., Off-axis bending behaviors and failure characterization of 3D woven composites, *Composite Structures* (2018), doi: https://doi.org/10.1016/j.compstruct.2018.10.009

Off-axis bending behaviors and failure characterization of 3D woven composites

Diantang Zhang*, Mengyao Sun, Xiaodong Liu, Xueliang Xiao, Kun Qian

Key Laboratory of Eco-Textiles, Ministry of Education, Jiangnan University, Wuxi 214122, China

Abstract:

This paper presents the influence of the off-axis angles on the flexure behaviors of three-dimensional (3D) woven carbon/epoxy composites. Four kind of samples with different angles, 0 degree, 30 degree, 45 degree and 90 degree, are experimentally tested via three-point bending method. The immersion focused ultrasound imaging and micro-computed tomography (Micro-CT) techniques are employed to investigate the deformation and damage mechanisms in the specimens fractured in bending. Results indicate that the stress-deflections of on-axis (0 degree and 90 degree) samples exhibit obvious quasi-brittle behaviors, whereas those of off-axis (30 degree and 45 degree) samples show important ductile features. Furthermore, the dominant failure mechanism of on-axis samples are identified to be inter-ply delamination and fiber bundle fractures, whereas those of off-axis samples are matrix cracks and tows debonding.

Keywords: 3D woven composites; Off-axis bending behaviors; Mechanical properties; Failure mechanism

1. Introduction:

3D woven preforms and their composites as structural components are being used increasingly for the aircraft and space applications owing to their excellent out-of-plane properties for delamination resistance and impact damage resistance [1-3]. In the past few years, researchers have mainly focused on the in-plane mechanical behaviors, while the bending large-deformation and failure mechanisms

* Corresponding author. Tel.: +8615961851268
E-mail address: zhangdiantang@jiangnan.edu.cn

are still systematically unclear. This can be attributed to the variability and complexity of the microstructure, and the limitation of the experimental technology. Furthermore, 3D woven composites are highly anisotropic, leading to the obvious orientation-dependence. In practice, 3D woven composite materials acquire the load carrying capacities not only along the two principal directions coinciding with the warp and weft axes, but also along any other bias directions. Consequently, an improved understanding of the off-axis bending behaviors and failure characterizations of 3D woven composites will be helpful for researchers in designing and constructing the high-performance materials.

3D woven composites are typically categorized as 3D angle-interlock woven composites and 3D orthogonal woven composites [2]. Especially, for 3D angle-interlock woven composites, a variety of structures can be derived by adjusting the fibrous configuration [4]. Moreover, the knowledge of the mechanical responses and the progressive failure characteristics of the woven architecture are ongoing subjects of research. As reviewed in the previous references, numerous experimental studies have been reported on the on-axis bending behaviors of 3D woven composites. For example, Kuo et al [5] examined the flexural behaviors of 3D woven carbon/carbon composites, and the results demonstrated that z-directional fibers can effectively arrest the delamination propagation. Umer et al [6] and Dai et al [7] conducted the detailed investigation of the flexural behaviors of 3D woven composites with different types of reinforcements such as orthogonal, angle interlock and layer to layer under three-point bending load. They found that the woven structures with angled binder tow show higher bending strength and modulus. They also noted that the failure mechanisms are importantly influenced by the woven patterns. Jin et al [8] discussed the three-point bending fatigue responses of 3D angle-interlock glass/polyester woven composites, and summarized that the dominant failure modes are determined by the cracks propagation and breakages of the warp yarns along the thickness direction. Pankow et al [9] reported that the flexural responses of two types of 3D woven textile composites, referred to as Z-fiber reinforcement and layer-to-layer architecture, using the End Notch Flexure tests.

Gerlach et al [10] addressed the delamination resistance of through-the-thickness angle interlock 3D woven carbon composites by using the three-point bending test. They concluded that the delamination lengths are mainly controlled by the binder density, and the test data are highly dependent on the support conditions and loading roller geometry.

From the above review of the previous studies, it is clear that the existed reports mainly have focused on the relationship between the fabric architectures and the macro-scale mechanical behaviors. In other words, the detailed damage processes and the micro-scale damage characterizations within the 3D woven composites cannot be effectively tracked and detected. As such, it is undoubtedly difficult to understand the final failure mechanism of 3D woven composites subjected to the bending loadings from the limited surface damage information. These shortcomings can be overcome with the use of the digital image correlation [11,12], acoustic emission [13] and micro-computed tomography (Micro-CT) [14,15] etc. For example, Zhang et al [16] conducted a digital image correlation (DIC) technique to evaluate the full-filed progressive damages and failure responses of hybrid 3D woven composites under the three-point bending loading. The experimental results suggest important architecture-dependent responses. More importantly, they concluded that the fiber tow kinking is a determining factor for the limited strength value of this materials. Recently, Turner et al [17] used Micro-CT to evaluate the collapse mechanisms of 3D orthogonal woven carbon composites subjected to the bending loading. However, the off-axis bending behaviors and failure mechanisms of 3D woven composites are rarely discussed. Thus, it is necessary to generate the reliable off-axis bending data for the design purposes.

In the present study, the bending mechanical behaviors of 3D woven angle-interlock carbon/epoxy composites with Four kind of samples with different angles, 0 degree, 30 degree, 45 degree and 90 degree, are investigated using three-point bending tests. The stress-deflection curves, maximum stress, initial modulus and strain to failure are recorded and discussed. Furthermore, the damage mechanisms are analyzed by using the immersion focused ultrasound scanning images

and Micro-CT graphs.

2. Experimental details

2.1 Materials and specimen preparation

The materials considered in this paper are 3D angle-interlock woven composites made of 3K/12K carbon fibers reinforcing TDE-86 epoxy matrix. Especially, the detailed weave style is a type of 3D angle-interlock woven reinforcement: warp-reinforced angle-interlock structure (see Figure 1) [18, 19]. The warp and weft are oriented along the x-direction and y-direction, respectively. The binder warp interlocks with the weft layers through the thickness (z-direction). Also, the warp and binder warp arrange alternately with a certain ratio of 1:1 along the x-direction. Therefore, this structure has two significant characteristics: (a) both the warp and weft remain straight to the maximal degree so as to make the fabric achieve higher in-plane mechanical properties, and (b) the fracture toughness of the thickness direction is improved due to the presence of the binder warp. Both the warp and weft are 12K carbon fiber, while the binder warp are 3K carbon fiber. Resin transfer mould (RTM) technique is used for the resin injection. A listing of the detailed parameters of 3D angle-interlock woven composites are provided in Table 1.

2.2 Three-point bending tests

It is well known that a complex stress state is experienced by 3D woven composites in flexural tests, with tensile, compressive and shear stresses are presented simultaneously in a loaded sample. In our previous study [18, 19], the stress distribution, strength and failure mechanisms of this class of 3D woven composites subjected to tensile and compressive loadings were importantly discussed by using numerical and experimental methods. In this paper, four kind of samples with different angles, 0°, 30°, 45° and 90°, are experimentally tested, as shown in Figure 2a. For the three-point bending tests, the standard test methods ASTM D790-10 are followed. The test samples are cut to the final dimensions of 80mm×15mm×4mm, and the span-to-depth ratio is 16:1, as depicted in Figure 2b. Also, in order to accurately characterize the effect of specimen geometry, the span-to-depth ratio samples of 8:1

are designed and tested [20-23]. All the tests are conducted on SHIMADZU AG-10KNE universal material machine at the room temperature. The speed of the indenter is 2mm/min. Each test result in this paper is the mean of three repeats. The load-deflection curves, maximum load and deflection to failure can be obtained.

Further, the nominal flexural stress (σ_f) and nominal initial modulus (E_f) can be calculated by

$$\sigma_f = \frac{3 \times P \times L}{2 \times b \times h^2}$$

$$E_f = \frac{L^3 \times \Delta P}{4 \times b \times h^3 \times \Delta S}$$

where L (mm) is the support span, and b (mm) and h (mm) are the width and thickness of the specimen. P (N) is the measured load. ΔP and ΔS are the load increment of initial line segment and the displacement increment of the middle point of the span, respectively. Here, it should be noted that the investigated 3D woven composites are more complicated that other reinforced plastics mentioned in ASTM D790-10. Hence, in order to eliminate the influence of the specimen geometry and test method, it is probably better to use the nominal flexural stress/initial modulus for the measured properties.

2.3 Water-logging ultrasonic testing

At present, non-destructive testing is a common practice for evaluating the material properties. Typically, the ultrasonic test method, making use of the principle of the sound-waves transmission, is becoming an increasingly popular analytical tool in measuring the interior damage of composite materials. Usually, all the damages result in the pores formation, which are the scattering of sound waves, in the composites. Also, there is a corresponding relation between the content of pores and the ultrasonic attenuation. When the sound-waves encounter the damage in the composite medium, C-scan/B-scan images with different colors, which can visually record the damage types, can be formed. The detailed relationships between the damage types and the image colors will be discussed in the later section.

In this paper, water-logging ultrasound scanning tests are conducted to acquire

the C/B-scan images of 3D woven composites after bending test by using SN-C3048 measuring device, as shown in Figure 3. In order to reduce the influence of the final curved specimen shape on the data measurements, the damage samples are firstly restored to the flat state, then placed in the sink. A focusing ultrasound probe which has a central ultrasonic frequency of 5MHZ, a wafer of 12.7mm, and a focal length of 50.8mm is used. Both the vertical and horizontal scanning speeds are 200mm/s, and the scanning step is 0.5mm. Here, the pores/defects exceeding 0.5mm can be identified from the method with a given ultrasonic frequency. Then the damage areas can be calculated based on the bottom echo wave information.

2.4 Micro-CT measures

Micro-CT is used to investigate the three-dimensional realizations of the failure mechanism in the tested 3D woven angle-interlock carbon/epoxy composites at micro-scale level (fiber tows/yarn level). Figure 4 presents the schematic of the cone-beam CT scan based on X-ray absorption. Micro-CT analysis are carried out on a diondo-d2. A 6μm resolution is used in this studies, with an accelerating voltage of 90kV and a beam current of 130μA. The flat panel detector is used in this work is 3072×3072 pixels with a pixel size of 139μm. The image acquisition time is about 1.5h per specimen. For 3D reconstruction, the images are acquired from 1600 rotation views over 360° of rotation (0.225° rotation step).

3. Results and Discussion

3.1 Off-axial bending mechanical behaviors

Figure 5 shows the nominal flexural stress-deflection diagrams of four kinds of angles samples, whose span-to-depth ratio is 16:1. Here, each curve is a representative sample for each orientation, and can provide a comprehensive depiction of the damage initiation and growth, as well as changes in the specimen stiffness. By comparison with four kinds of angles of specimens, the stress-deflection curves clearly show obviously different trends, indicating that the bending mechanical behaviors are sensitive to the off-axial orientation. Also, this phenomenon demonstrates that with the change of the off-axis angle, the damage processes and

failure modes are importantly different. For 0 degree (weft) and 90 degree (warp) on-axis specimens, the stress-deflection curves are almost linear up to the catastrophic failure, suggesting an important brittle behavior [20, 21]. This reason is that in the on-axis samples, the applied loads are directly related to the transverse properties of carbon fiber bundles. This result can also be found in Ref [24]. Moreover, it can be observed that the stress suddenly drops at 90% of the ultimate strength in the 90 degree sample, which can be attributed to the critical structural damage. Unlike 90 degree sample, 0 degree one shows some small fluctuations before reaching the ultimate fracture. For both 30 degree and 45 degree off-axis samples, the stress-deflection curves exhibit non-linear trends, obtaining a larger bending deflection and a lower maximum load. This behavior displays a ductile feature, and can be explained as a result of the matrix-dominated character, which is consistent with the behavior observed by Gerlach et al [10] and Tumer et al [17]. Especially, 45 degree samples undergo a longer yield stage than 30 degree ones. Also, the stress-deflection curves of 30 degree and 45 degree samples are smooth, indicating that no catastrophic damages suddenly occur.

In addition, it is worth noting that the nominal stress-deflection curves show an obvious geometry-dependency [22, 23]. As compared to with the larger span-to-depth ratio samples (16:1), the shorter span-to-depth ratio samples (8:1) present significant linear segments before the maximum stress indicates hardening elastic responses and increased brittleness. Namely, changing specimen geometry influences specimen brittleness, which indicates material quasi-brittleness.

For better interpretation of the experimental results, the key bending parameters including the nominal maximum stress, nominal initial modulus and failure strain for four kinds of angles samples are summarized in Figure 6-8, respectively. Here, each value is the average of three samples tested, and the Standard Deviation (SD) is also presented in Figure 6-8.

Clearly, all the observed results suggest obvious anisotropic characteristics. From Figure 6, it shows that for four kind of samples with different off-axis angles, 0 degree, 30 degree, 45 degree and 90 degree, the nominal maximum stresses are 960.41MPa,

480.61MPa, 422.71MPa and 1020.21MPa, respectively. It can be concluded that the nominal maximum stress of 90 degree specimen is slightly higher than that of 0 degree specimen. On the one hand, this is mainly because of the little difference of the end/pick count in the warp and weft directions. Apart from the structural parameters, the binder warp is also responsible for the nominal maximum stress. Namely, for 90 degree sample, the crimped binder warps below the specimen's neutral plane subjected to tension are perpendicular to the indenter, and try to straighten under the bending load, resulting in an increasing value. In contrary, the nominal maximum stresses of off-axis samples (30 degree and 45 degree) are relative lower as compared to those of on-axis samples (0 degree and 90 degree). Unsurprisingly, the main cause, in fact, is that under the bending loading, the bottom warp/binder warp and weft of on-axis samples experience the maximum tensile stress. However, for the off-axis samples, warp and weft are biased with certain angle. As a result, when subjected to shear loading, these off-axis samples try to reorient towards the principal loading axis. Thus, the off-axis samples firstly occur large geometrical deformation to adjust themselves and change the spatial position which certainly will lead to the interfacial debonding between the yarns and matrix, which will be verified in Section 3.2. This result can also be found in Ref [3]. They suggested that during the reorientation process, the so-called “scissoring effect”, which is also usually referred to as fiber trellising [25], occurs between warp and weft. This behaviors results in the large deformation. Furthermore, when the off-axis angle reaches 45 degree, this phenomenon is particularly evident.

As shown in Figure 7, the nominal initial modulus of 90 degree sample (84.15GPa) exceeded that of 0 degree sample (81.60GPa) by 3.13%, that of 30 degree sample (39.96GPa) by 110.19% and that of 45 degree sample (26.77GPa) by 214.44%, which are consistent with the trends of the nominal maximum stresses. Generally, the nominal initial modulus is directly related to the surface rigidity near the loading head. As mentioned before, the upper surfaces of on-axis samples maintain the straight warp/weft alignment inside the composite structure, leading to higher initial in-plane stiffness. However, for off-axis samples, the three main load-carrying tows are not

fully utilized, which result in lower flexural modulus.

In Figure 8, it is interesting to see that ranking for the strains to the maximum stress are different, i.e., 45 degree>30 degree>90 degree>0 degree, which is almost contrary to the sequence of the flexural strength and initial modulus. The main cause for this may lies in the bending coordination mechanism of the structure.

The energy absorbed per unit volume up to fracture (in MJ/m^3) is calculated as the area under the load-displacement curve, as shown in Table 2. Obviously, the off-axis angle has an important influence on the energy absorption of 3D woven composites subjected to the bending load. The energy absorption of 45° sample (3.50 MJ/m^3) exceeds that of 0° sample (1.09 MJ/m^3) by 224.78%, that of 30° sample (2.93 MJ/m^3) by 19.45% and that of 90° sample (1.54 MJ/m^3) by 127.27%. Apparently, compared with the on-axis samples, the off-axis ones show greater energy absorption. This phenomenon can also be explained by the scissoring effect as mentioned earlier [3]. The above findings indicate that this class of off-axis materials can be considered as a good candidate for the impact resistance, where the energy absorption is of prime interest. Considerably enhanced impact properties can be expected. This result agrees with the findings reported in Ref [26].

3.2 Analysis of failure characterization in tested composites

As the main of the study is to investigate the off-axis bending failure characterization of 3D angle-interlock woven composites, four kind of samples with different angles tested under bending conditions are carried out employing both water-logging ultrasonic and micro-CT techniques.

3.2.1 Water-logging ultrasonic imaging analyses

To investigate intuitively the damage behaviors of the specimens, the water-logging ultrasonic setup is used to capture the images of the whole (C-scan, x-y plane) and centre (B-scan, x-z plane) of the specimens. It should be noted that the image designation strips indicate the intensity of the reflected wave. Namely, from blue (0) to red (100), the reflected wave enhances, suggesting different damage modes. Typically, (1) when the incident wave encounters the internal damage/defect, the reflected wave weakens and the damage point is "navy blue"; (2) when the incident

wave encounters the resin rich zone, the reflected weave strengths and the damage point is "red" or "yellow"; (3) the undamage point generally is wathet or green.

Figure 9-12 presents the C-scan and B-scan images of four kinds of angles samples. Clearly, the ability of this method to capture the full-field and local damage distributions is importantly presented. From all the C-scan images, it can be observed by the naked eyes that the external morphology of on-axis samples (see figure 13(a) and (d)) are completely fracture, while those of off-axis ones (see figure 13(b) and (c)) are not serious. However, with 30% of the received echo amplitude as the threshold, the calculated damage area proportion of four kind of samples with different angles, 0 degree, 30 degree, 45 degree and 90 degree are 24.0%, 40.2%, 50.1% and 30.1%, respectively. This also can be verified visually by the C-scan images. Namely, the damage regions near the point of the loading head are navy blue. This phenomenon can be explained by that unlike on-axis samples, off-axis samples are capable to produce a larger bending deflection, and thus result in the greater damage areas.

Furthermore, to investigate the damage details of the specimens below the indenter and away from the loading point, B-scan technology is used to capture the images of the through-thickness surface of the samples. It can be clearly seen that B-scan results provide more abundant information as compared to C-scan ones. For B-scan results of four kinds of angles samples, there are two similar characteristics: (1) The central deep blue regions show distinct triangle for all the samples. This suggests that the damages spread from the compressive center to the around. And with the thickness increasing, damage spreading scopes increase; (2) Based on the observed imaging features, the sample can be divided into two different parts, including the top plies and the bottom plies, along the thickness direction. In the top plies below the indenter, it can be observed that four colors, blue, green, red and yellow, appear speckled distribution. This can be attributed to the compressive failure, including the kinking, micro-buckling, fiber bundles crack, matrix crack etc. In the bottom plies, there are some strips of the navy blue area. This is because that the yarn bundles in the bottom plies are mainly subjected to the tensile load, resulting in the fiber bundles fracture and inter-ply delamination.

Although the above water-logging ultrasonic technique demonstrates the macro- and meso-scales damage distribution, it does not provide precise information about their internal damage characteristics such as tow debonding, ply facture, matrix cracks and fiber bundles failure.

3.2.2 Micro-CT tomography analyses

To further understand the underlying damage mechanism, the reconstructing 3D images and 2D cross-sectional slices, with help of Micro-CT technique, of the ultimate fracture of four kinds of angles samples are presented in Figure 14-17. Typically, the common failures include kink band forms under the loading head and the fiber bundle cracks in the bottom. Specifically, the kink bands progressively develop on the compressive side of the specimens with further deformation, limiting the initial modulus of the materials. Many researchers reported this phenomenon, and concluded that the kink band formation is due to both fiber misalignment and matrix degradation [27, 28]. Also, the fiber bundle cracks are due to tensile in the bottom. Besides, the failure modes of four angles of samples show important differences.

From Figure 14a, it can be clearly observed that the macroscopic failure of 0 degree sample is totally dominated by the shear fracture with the splitting phenomenon. As shown in Figure 14b and 14c, the major damage modes observed at meso-scale are kinking, cracking in the weft, cracking in the warp, cracking in the binder warp, matrix crack, tows debonding, intra-ply delamination and fiber bundles fracture. The displayed result in Figure 14b is consistent with that of B-scanning in Figure 9. This shows that B-scanning images are able to capture the local damage events. In fact, the weft is the only tows to have a straight orientation to subject the flexure loading. This thereby results in the brittle failure and lower deflection, as mentioned earlier. Zhang et al [16] reported the progressive damage and failure response of 3D woven composites subjected to the bending loads through a series of images taken on the polished front surface. The kind bandings are firstly found in the SEM image. Therefore, a reasonable inference can be refined that after the initial loading, the evolution of kink banding leads to the high shear strain localization near the point of the loading head, which causes the surrounding matrix/weft firstly to

crack. Then the main crack traverses through the matrix/warp/binder warp/interface to propagate to another weft. In this loading process, the matrix, warp and binder warp experience the inter-tows cracking. More importantly, intra-ply delamination between wefts, which is also clearly seen in the microscopic image, is developed. Totally, it can be asserted that for 0 degree sample, inter-ply delamination and weft fracture are the prominent damage modes.

Unlike the result of 0 degree sample, there are no catastrophic and continuous cracks for 30 degree sample, as shown in Figure 15a. The conclusion is consistent with the results of Figure 5. That is the inflection points on the corresponding stress-deflection curves display the damage generation and propagation. From Figure 15b and 15c, the observed damage modes mainly include kinking, cracks in matrix/weft/warp, tows debonding and fiber bundles fracture. Moreover, no apparent delamination are found. This is a considerable shift as compared to 0 degree sample (weft direction). In addition, the failure location is focused on the edge of width direction. In fact, this is the off-axis orientation that the warp, weft and binder warp all bear bending loads, which mainly make the crack extend along the in-plane fiber bundles until the sample edges and also provide additional resistance to crack propagation along the thickness direction. Again, this allows for the large-deflection to increase, but it is also able to withstand significantly lower load. From Figure 16, it can be noticed that the failure characteristics of 45 degree sample show a very similar trend with that of 30 degree sample, except more tows debonding at the bottom. This also explains why the strength of 45 degree sample is lower than that of 30 degree sample as described earlier.

As can be seen from Figure 17, 90 degree samples exhibit catastrophic failure by combination of delamination splitting and crushing into small fragments. In detail, these cracks are followed by kinking, cracking in weft, fracture in the warp and binder warp, matrix crack, tows debonding, intra-ply delamination and fiber bundles fracture. It can be clearly observed that 90 degree samples show more serious damage as compared to 0 degree sample. This is mainly attributed to the existence of binder warp in the through-thickness, which has the layer connect function and tends to be

straight.

Conclusions

3D woven angle-interlock composites have excellent enhanced inter-laminar performance over 2D woven composite laminates and hence are increasing favored for the aircraft and space applications. In the current study, experimental investigations are carried out to assess the effects of off-axis directions on the flexure mechanical behaviors and failure mechanism of 3D woven angle-interlock carbon/epoxy composites. Based on the detailed analysis, following conclusions are made:

1) Compared to 0 degree and 90 degree samples, 30 degree and 45 degree samples show lower flexure strength, initial modulus and larger flexure deflection. Also, the stress-deflections of 0 degree and 90 degree samples exhibit an obvious quasi-brittle behavior, whereas that of 30 degree and 45 degree samples show an important ductile feature.

2) With 30% of the received echo amplitude as the threshold, the calculated damage area proportions of off-axis samples are larger than that of on-axis samples. This phenomenon is because that off-axis samples are capable to produce a larger bending deflection.

3) Under the flexural loading, 30 degree and 45 degree off-axis samples show small localized cracks with little delamination. However, 0 degree and 90 degree on-axis samples exhibit serious damages, mainly including the inter-ply delamination and fiber bundles fracture.

For afore-mentioned results, further study is expected to examine how the manipulation and design of wide range of off-axis angles can optimize the maximum stress, dissipation, and damage initiation/evolution. More importantly, developing a reasonable mechanical theory is promising to be exploited for the evaluation of anisotropy characteristics of 3D woven composites.

Acknowledgements

The authors gratefully acknowledge the financial support from Natural Science Foundation of China (No. 11702115), Natural Science Foundation of Jiangsu Province (P.R.China) (No. BK20170166) and Natural Science Foundation Central Universities (No. JUSRP11703 and JUSRP51718A).

References

[1] Mouritz AP ,Bannister MK, Falzon PJ, Leong KH. Review of applications for advanced three-dimensional fiber textile composites. Compos Part A Appl Sci Manuf 1999;30:1445-1461.

[2] Ansar M, Wang XW, Zhou CW. Modeling strategies of 3D woven composites: A review. Compos Struct 2011;93:1947-1963.

[3] Liu G, Zhang L, Guo LC, Wang QM, Liao F. A modified V-notched beam test method for interlaminar shear behavior of 3D woven composites. Compos Struct 2017;181:46-57.

[4] Zhang DT, Chen L, Wang YJ, Zhang LK, Zhang YF, Yu KJ, Lu XF, Sun J, Xiao XL, Qian K. Stress field distribution of warp-reinforced 2.5D woven composites using an idealized meso-scale voexl-based model. J Mater Sci 2017;52:6814-6836.

[5] Kuo WS, Ko TH, Cheng KB, Hsieh KY. Flexural behavior of three-axis woven carbon/cabon composites. J Mater Sci. 2001;36:2743-2752.

[6] Umer R, Alhussein H, Zhou J, Cantwell WJ. The mechanical properties of 3D woven composites. J Compos Mater 2017;51:1703-1716.

[7] Dai S, Cunningham PR, Marshall S, Silva C. Influence of fibre architecture on the tensile, compressive and flexural behavior of 3D woven composites. Compos Part A Appl Sci Manuf 2015;69:195-207.

[8] Jin LM, Hu H, Sun BZ, Gu BH. Three-point bending fatigue behavior of 3D angle-interlock woven composite. J Compos Mater. 2012;46:883-894.

[9] Pankow M, Salvi A, Waas AM, Yen CF, Ghiorse S. Resistance to delamination of 3D woven textile composites evaluated using End Notch Flexure (ENF) tests: Experimental results. Compos Part A Appl Sci Manuf 2011;42:1463-1476.

[10] Gerlach R, Siviour CR, Wiegand J, Petrinic N. In-plane and through-thickness properties, failure modes, damage and delamination in 3D woven carbon fibre composites subjected to impact loading. Compos Sci Technol 2012;72:397-411.

[11] Zheng YY, Sun Y, Li JL, Liu LM, Chen L, Liu JL, Tian SQ. Tensile response of carbon-aramid hybrid 3D braided composites. Mater Des 2017;116:246-252.

[12] Pan B, Yu LP, Yang YQ, Song WD, Guo LC. Full-field transient 3D deformation measurement of 3D braided composite panels during ballistic impact using single-camera high-speed stereo-digital image correlation. Compos Struct 2016;157:25-32.

[13] Lomov SV, Karahan M, Bogdanovich AE, Verpoest I. Monitoring of acoustic emission damage during tensile loading of 3D woven carbon/epoxy compsoites. Text Res J 2014;84:1373-1384.

[14] Liu Y, Straumit I, Vasiukov D, Lomov SV, Panier S. Prediction of linear and non-linear behavior of 3D woven composite using mesoscopic voxel models reconstructed from X-ray micro-tomography. Compos Struct 2017;179:568-579.

[15] Pazmino J, Carvelli V, Lomov SV. Micro-CT analysis of the internal deformed geometry of a non-crimp 3D orthogonal weave E-glass composite reinforcement. Compos Part B Eng 2014;65:147-157.

[16] Zhang DY, Waas AM, Yen CF. Progressive damage and failure response of hybrid 3D textile composites subjected to flexural loading, part I: Experimental studies. Int J Solids Struct 2015;75-76:309-320.

[17] Turner P, Liu T, Zeng X. Collapse of 3D orthogonal woven carbon fibre composites under in-plane tension/compression and out-of-plane bending. Compos Struct 2016;142:286-297.

[18] Zhang DT, Chen L, Wang YJ, Zhang LK, Zhang YF, Yu KJ, Lu XF, Sun J, Xiao XL, Qian K. Stress field distribution of warp-reinforced 2.5D woven composites using an idealized meso-scale voxel-based model. J Mater Sci 2017;52:6814-6836.

[19] Zhang DT, Chen L, Wang YJ, Jia N, Qian K. Finite element analysis of warp-reinforced 2.5D woven composites based on a meso-scale voxel model

under compression loading. Appl Compos Mater 2017;24:911-929.

[20] Salviato M, Kirane K, Ashari SE, Bažant ZP, Cusatis G. Experimental and numerical investigation of intra-laminar energy dissipation and size effect in two-dimensional textile composites. Compos Sci Technol 2016;135:67-75.

[21] Salviato M, Chau VT, Li WX, Bažant ZP, Cusatis G. Direct testing of gradual postpeak softening of fracture specimens of fiber composites stabilized by enhanced grip stiffness and mass. J Appl Mech 2016;83:111003-1-10.

[22] Tang T, Bažant ZP, Yang S, Zollinger D. Variable-notch one-size test method for fracture energy and process zone length. Eng Fract Mech. 1996;55(3):383–404.

[23] Li W, Jin Z, Cusatis G. Size effect analysis for the characterization of Marcellus shale quasi-brittle fracture properties. Rock Mech Rock Eng. 2018, https://doi.org/10.1007/s00603-018-1570-6.

[24] Ullah H, Harland AR, Silberschmidt VV. Characterisation of mechanical behaviour and damage analysis of 2D woven composites under bending. Compos Part B Eng 2015;75:156-166.

[25] Hufner DR, Michael LA, A progressive failure theory for woven polyer-based composites subjected to dynamic loading. Compos Struct 2009;89:177-185.

[26] Glud JA, Dulieu-Barton JM, Thomsen OT, Overgaad LCT. Fatigue damage evolution in GFRP laminates with constrained off-axis plies. Compos Part A Appl Sci Manuf 2017;95:359-369.

[27] Saleh MN, Yudhanto A, Potluri P, Lubineau G, Soutis C. Characterising the loading direction sensitivity of 3D woven composites: Effect of z-binder architecture. Compos Part A Appl Sci Manuf 2016;90:577-588.

[28] Ary Subagia IDG, Kim Y, Tijing LD, Kim CS, Shon HK. Effect of stacking sequence on the flexural properties of hybrid composites reinforced with carbon and basalt fibers. Compos Part B Eng 2014;58:251-258.

Figures:

Tables:

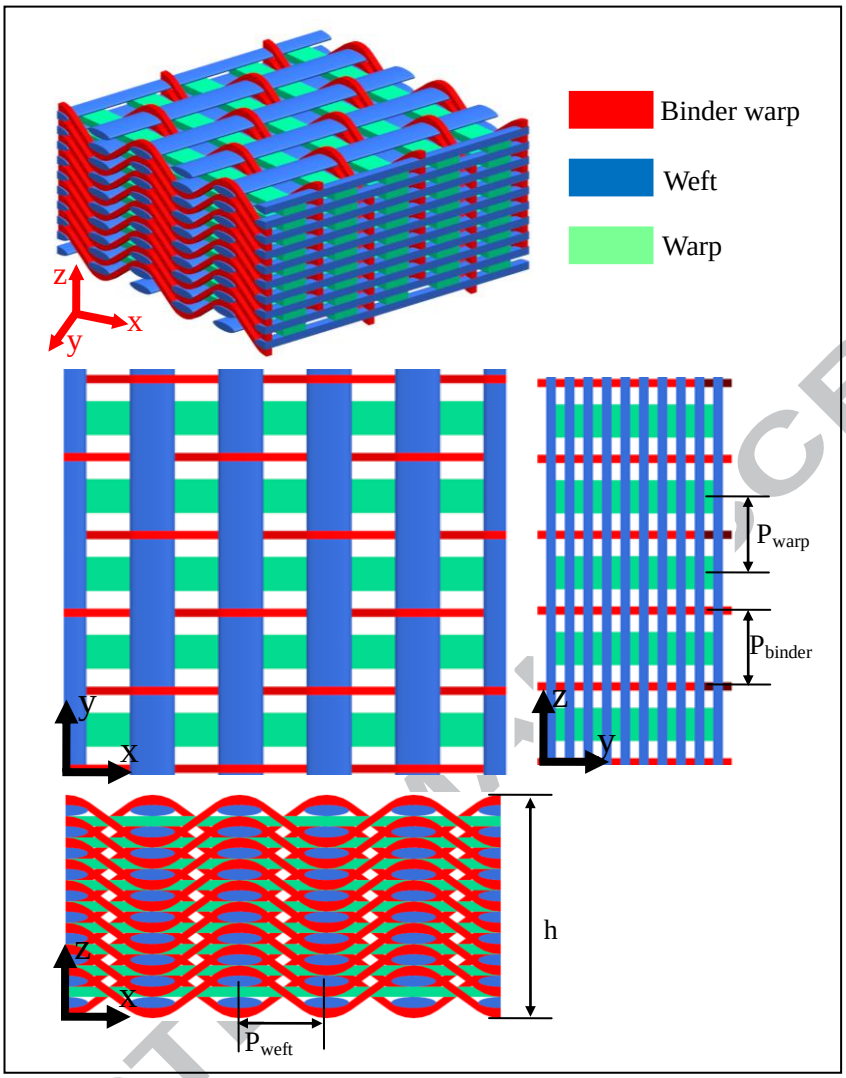

Fig. 1. Schematic of woven angle-interlock structure

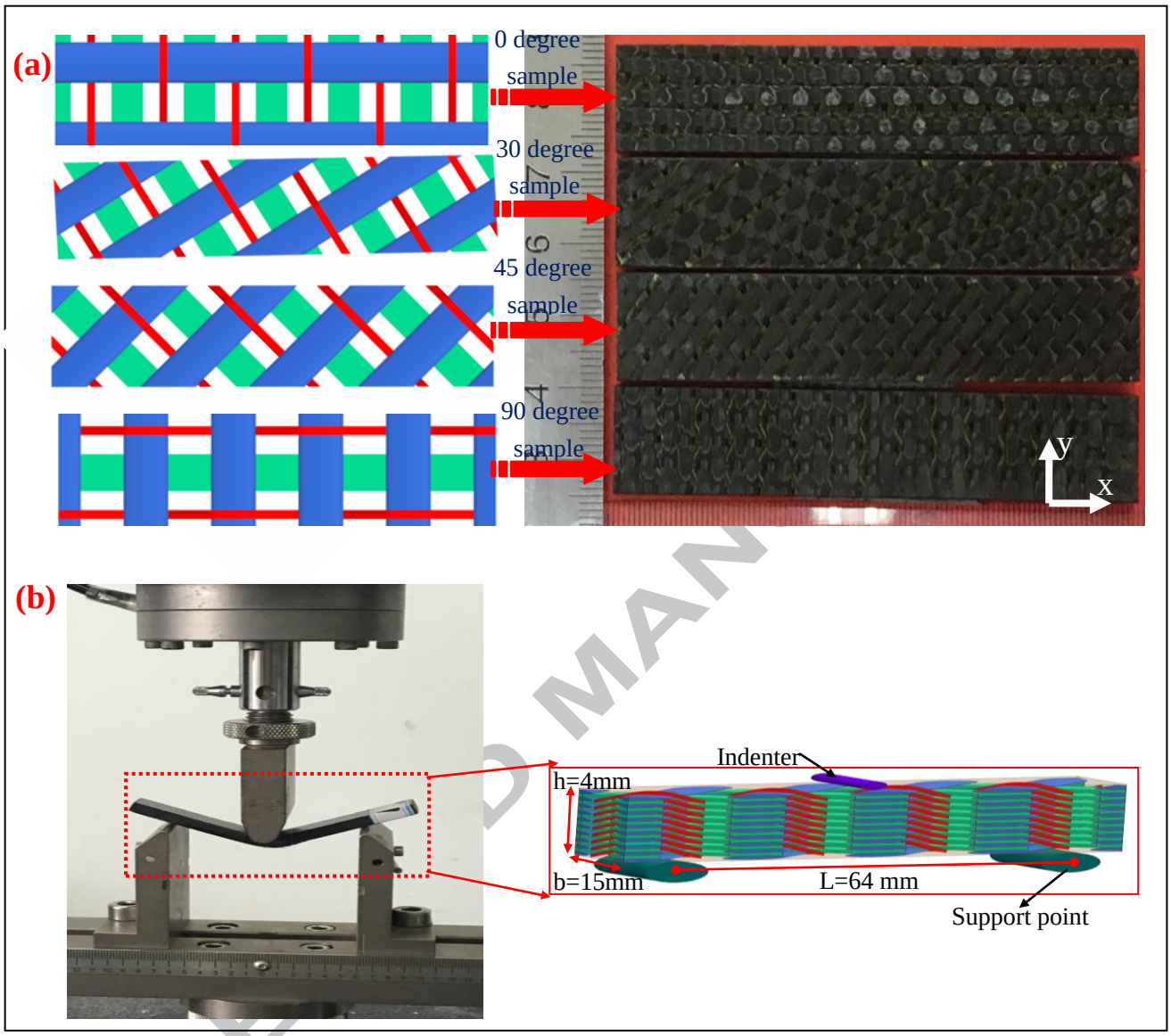

Fig. 2. Flexure test samples (a) and three-points flexure setup (b)

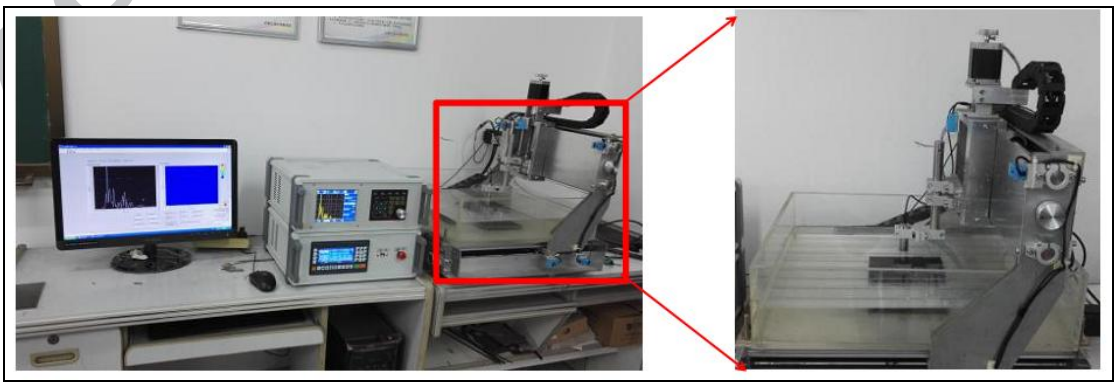

Fig. 3. Immersion focused ultrasound setup

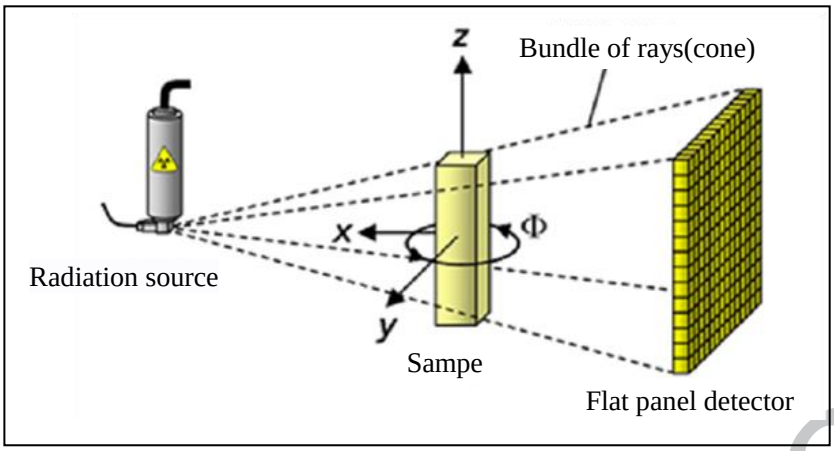

Fig. 4. Schematic of micro-computed tomography setup

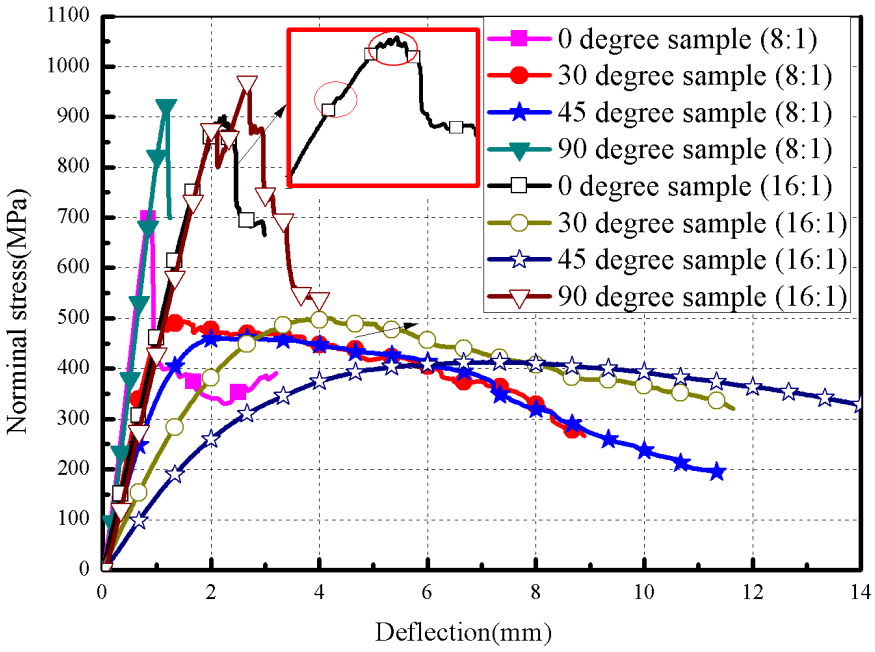

Fig. 5. Nominal stress-deflection curves of four kinds of angles samples

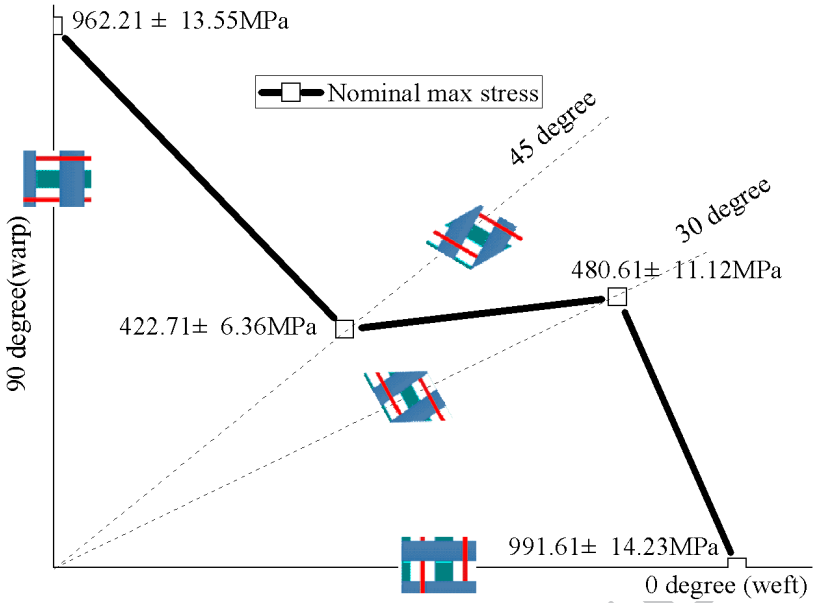

Fig. 6. Nominal max stress of four kinds of angles samples

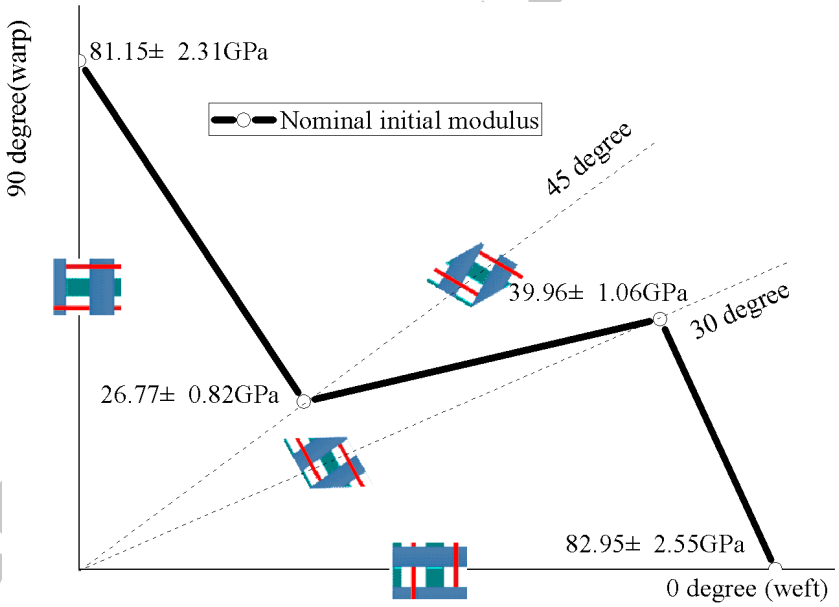

Fig. 7. Nominal initial modulus of four kinds of angles samples

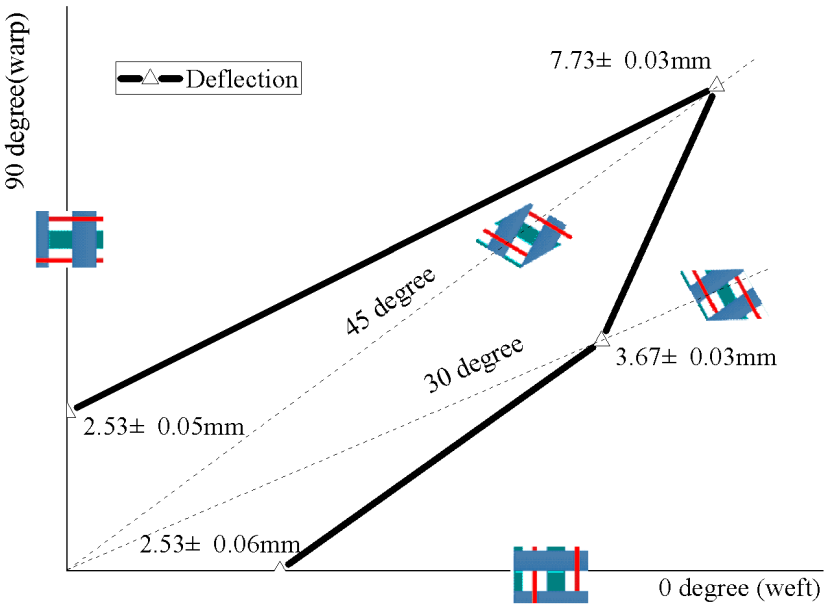

Fig. 8. Failure deflection of four kinds of angles samples

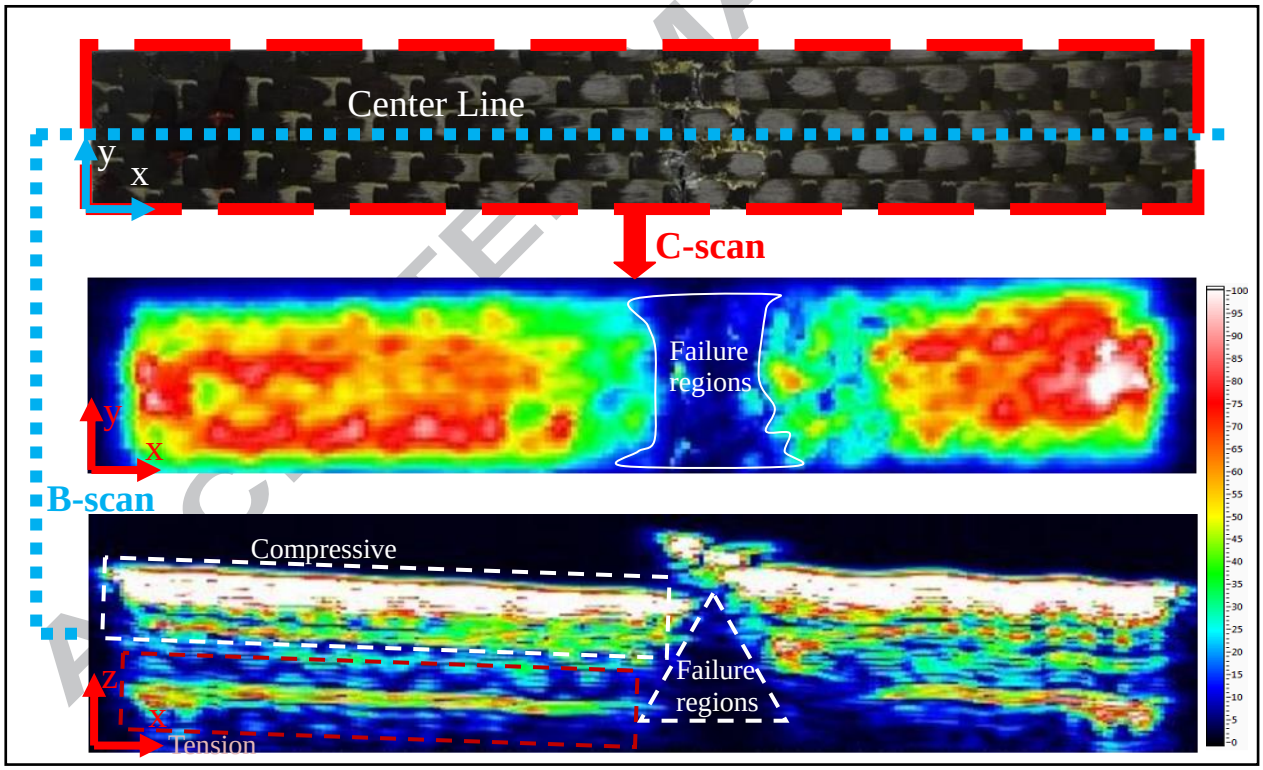

Fig. 9. Ultrasound scanning images of 0 degree sample

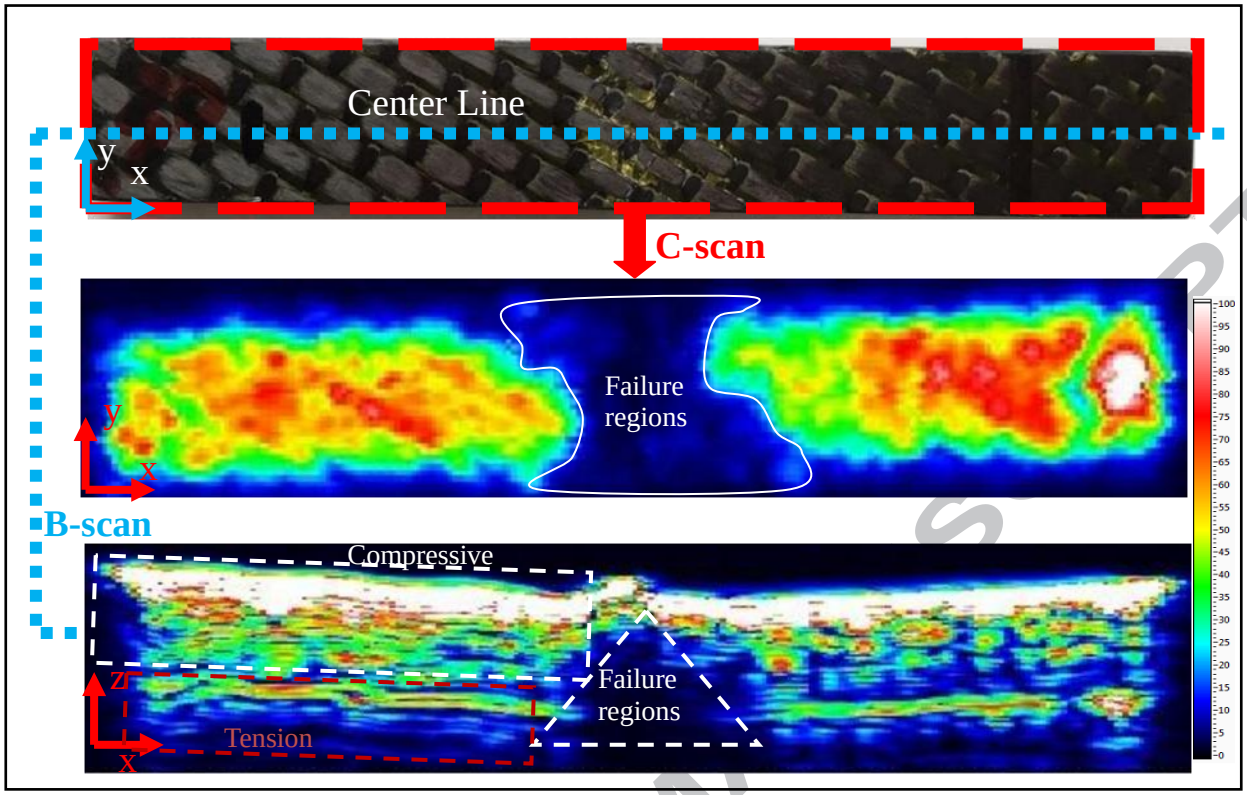

Fig. 10. Ultrasound scanning images of 30 degree sample

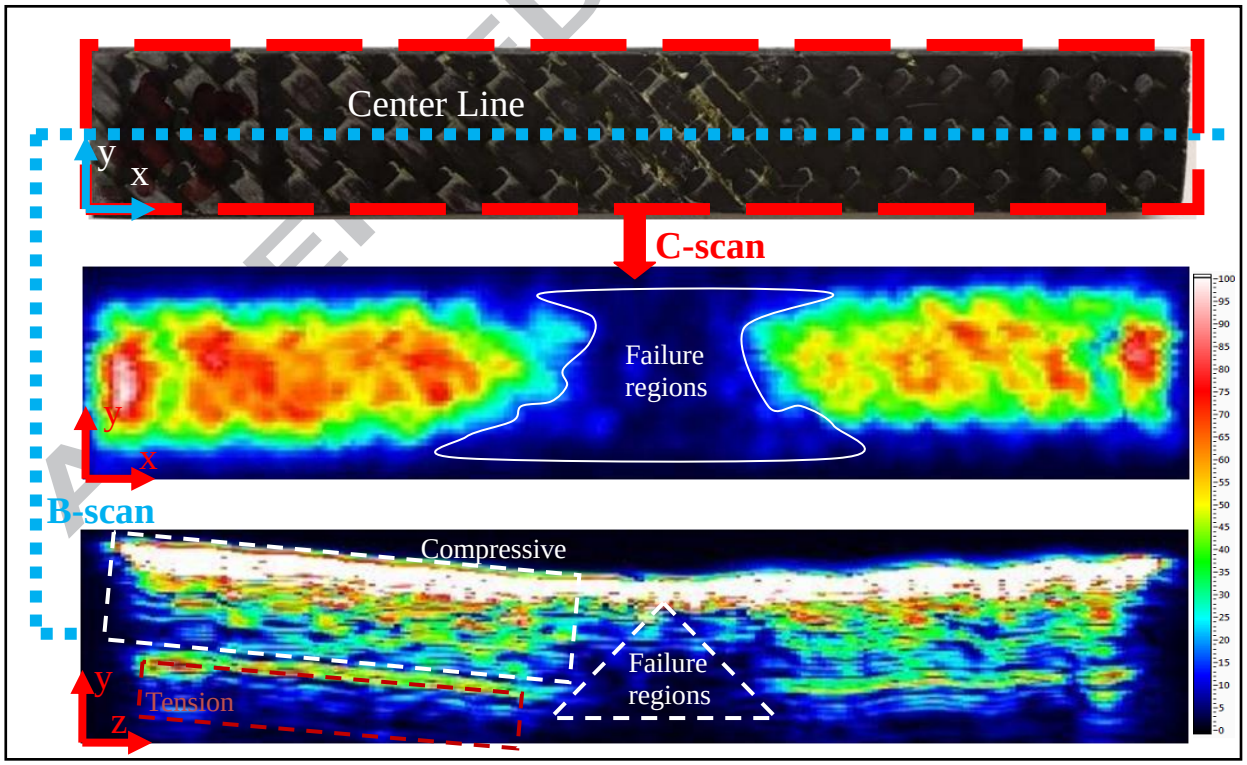

Fig. 11. Ultrasound scanning images of 45 degree sample

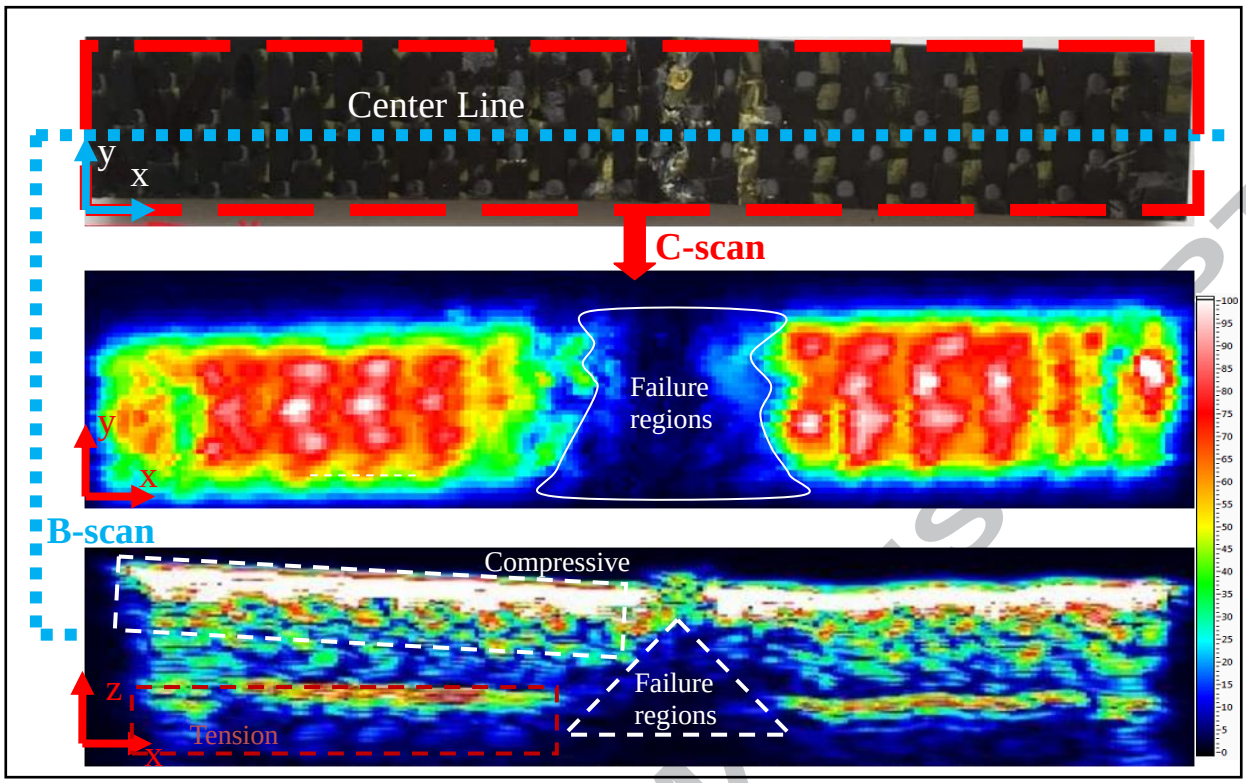

Fig. 12. Ultrasound scanning images of 90 degree sample

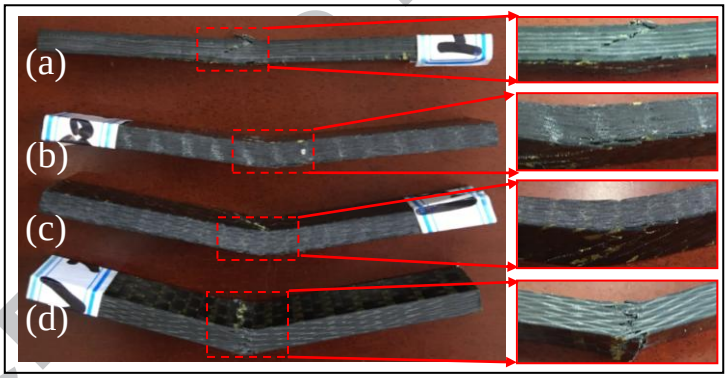

Fig. 13. Macro failure modes of 0 degree sample (a), 30 degree sample (b), 45 degree sample (c) and 90 degree sample (d)

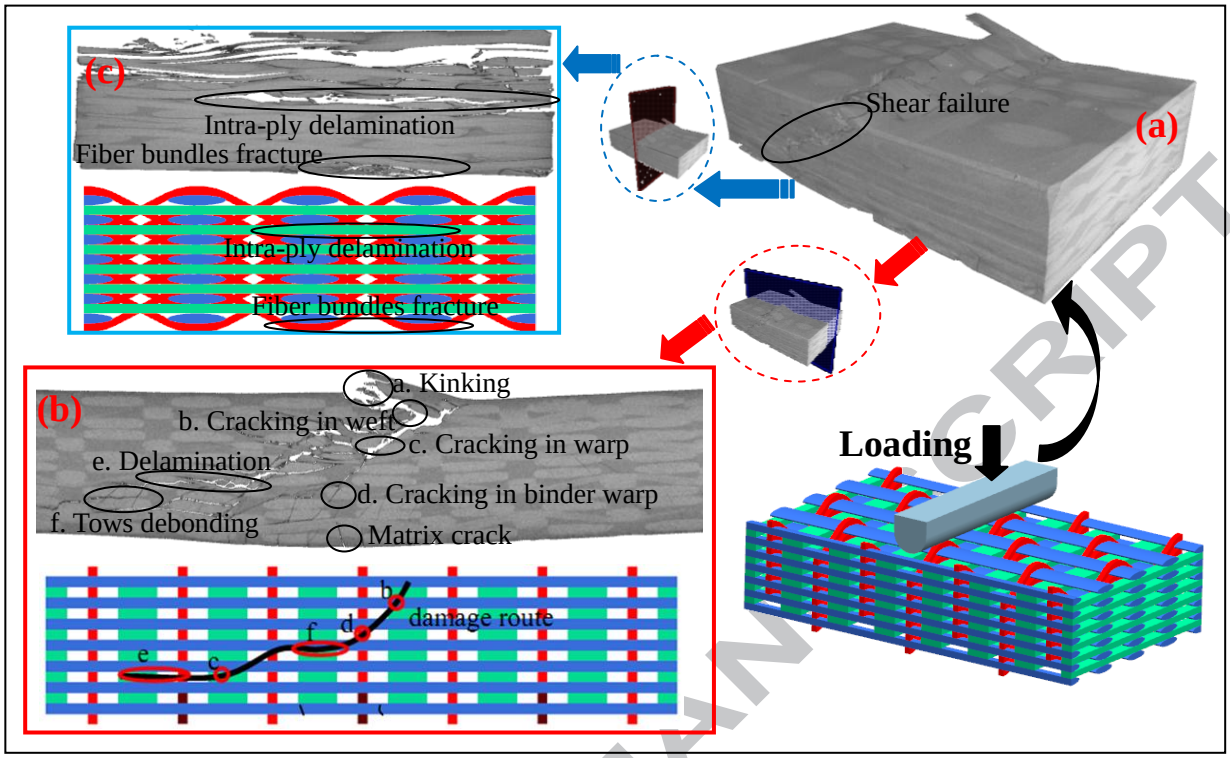

Fig. 14. Micro failure modes of 0 degree sample

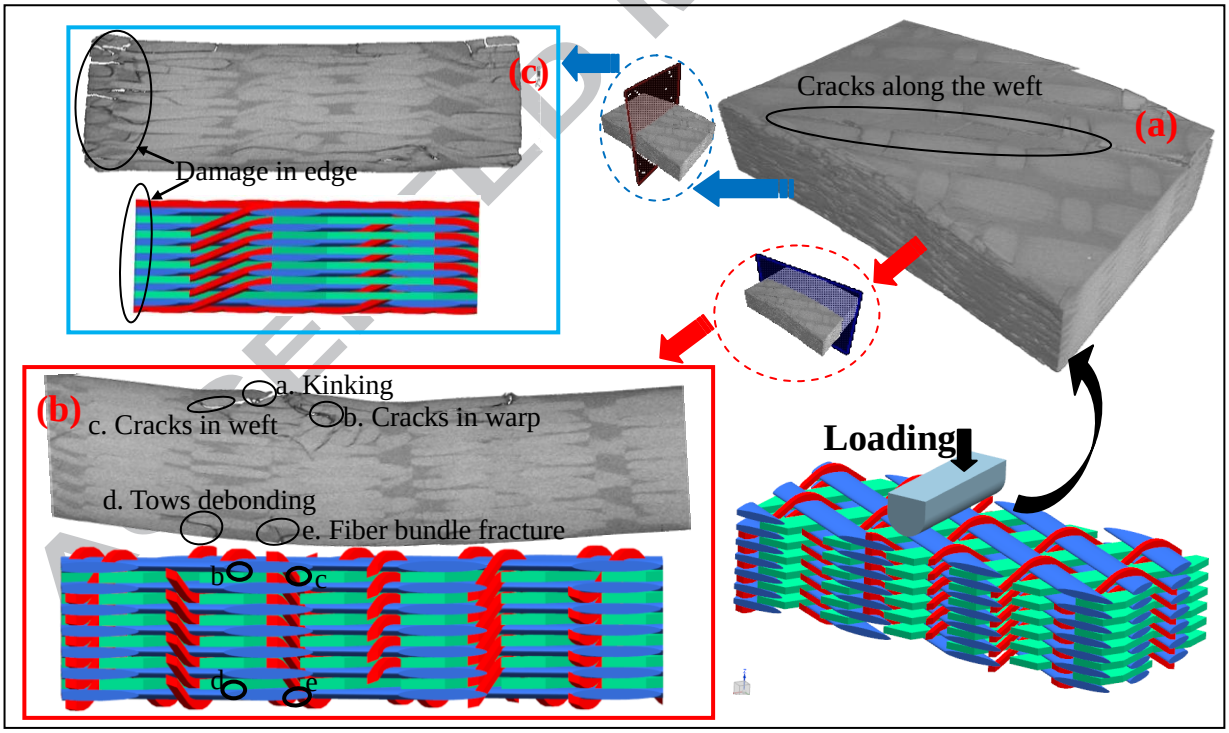

Fig. 15. Micro failure modes of 30 degree sample

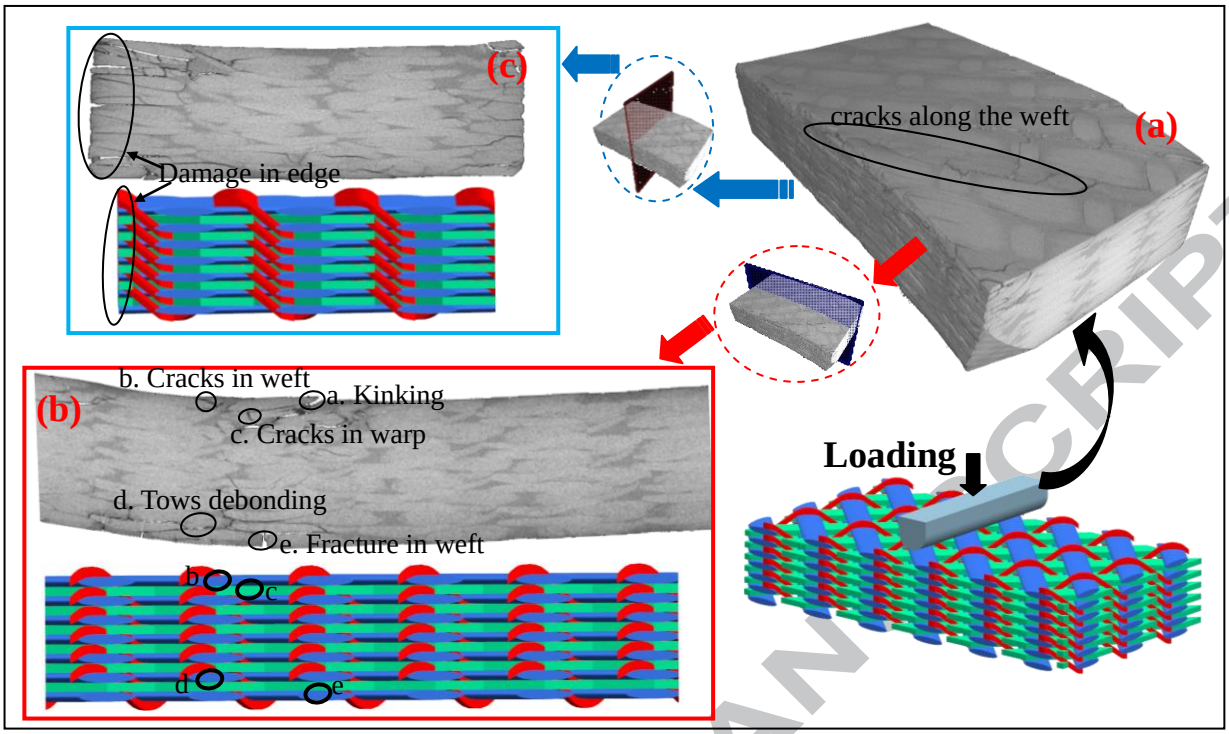

Fig. 16. Micro failure modes of 45 degree sample

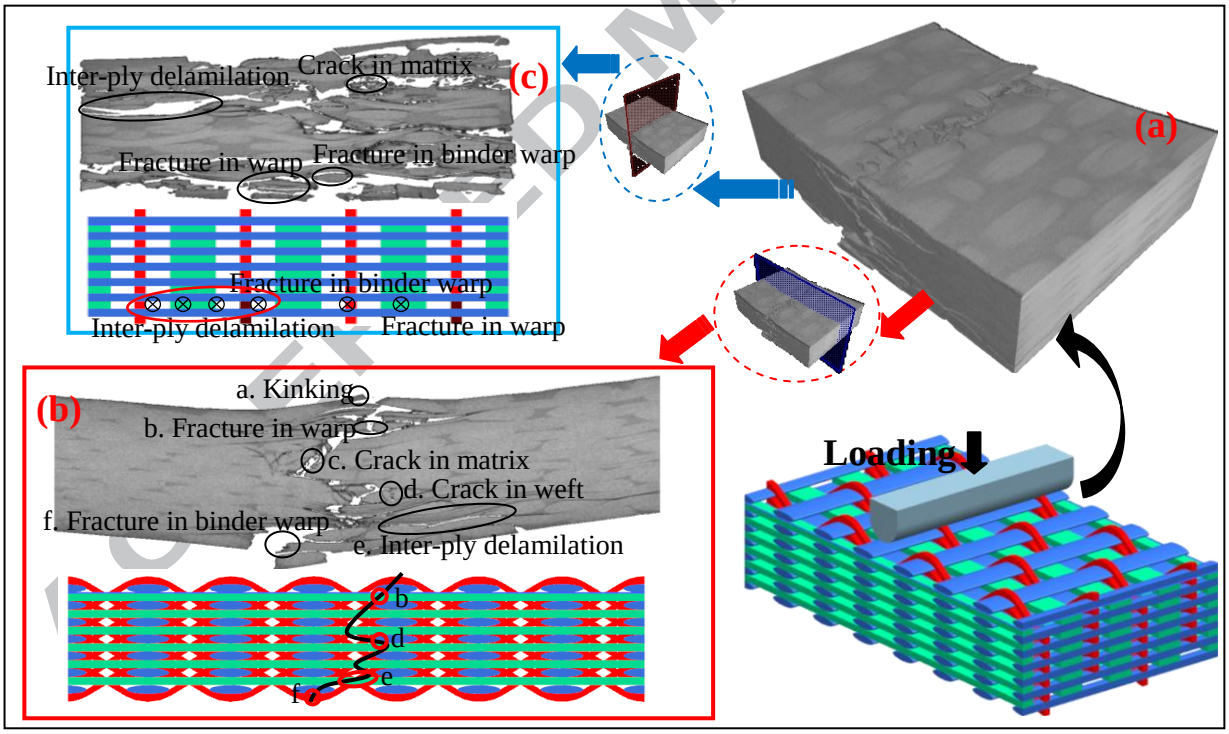

Fig. 17. Micro failure modes of 90 degree sample

Table 1 The detailed parameters of 3D angle-interlock woven composites

Parameters	Symbols	Values
Number of layers	*n*	8
Thickness(mm)	*h*	4
Yarn density (tows /cm)	P_{warp}, P_{weft}, P_{binder}	3, 3, 3
Yarn fineness(K)	*Warp, weft, binder warp*	800, 800, 200
Fiber volume fraction(%)	V_{total}, V_{warp}, V_{weft}, V_{binder}	50.90, 21.61, 21.21, 8.08

Table 2 Energy absorption of four kinds of angles samples

Off-axis angle (degree)	Energy absorption (MJ/m^3)
0	1.09±2.76%
30	2.93±1.89%
45	3.50±0.59%
90	1.54±3.39%